Characterizing two types of transient intraseasonal oscillations in the Eastern Tibetan Plateau summer rainfall

Jing Yang, Qing Bao, Bin Wang, Haozhe He, Miaoni Gao & Daoyi Gong

Climate Dynamics
Observational, Theoretical and Computational Research on the Climate System

ISSN 0930-7575
Volume 48
Combined 5-6

Clim Dyn (2017) 48:1749-1768
DOI 10.1007/s00382-016-3170-z

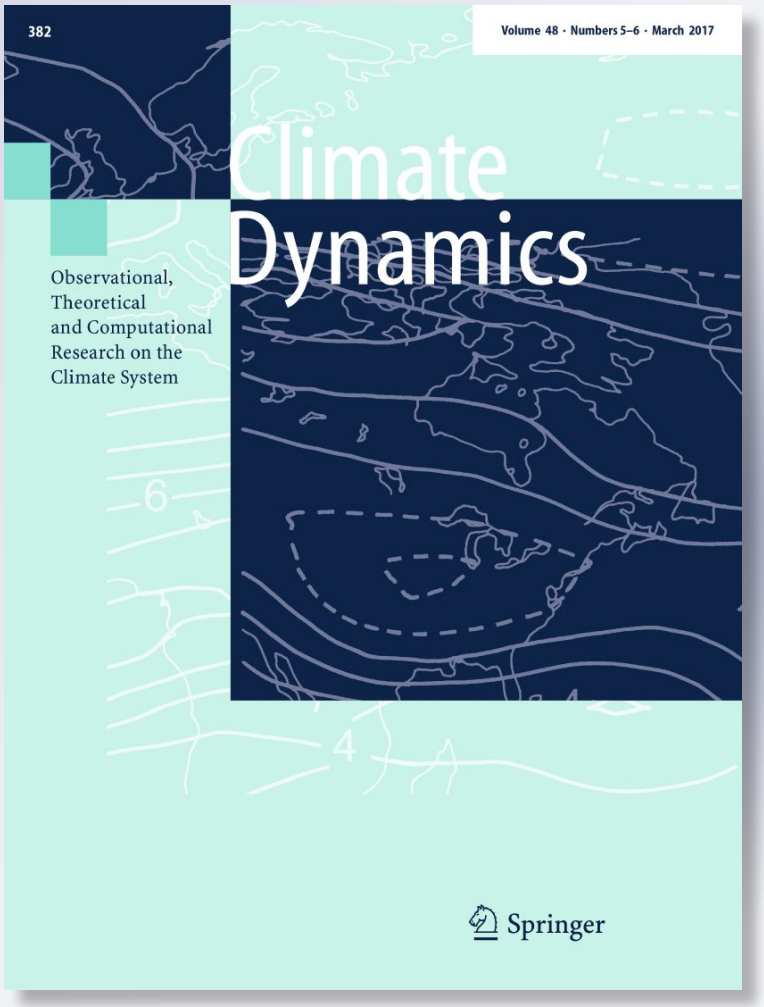

Springer

Clim Dyn (2017) 48:1749–1768
DOI 10.1007/s00382-016-3170-z

Characterizing two types of transient intraseasonal oscillations in the Eastern Tibetan Plateau summer rainfall

Jing Yang[1] · Qing Bao[2] · Bin Wang[3,4] · Haozhe He[1] · Miaoni Gao[1] · Daoyi Gong[1]

Received: 3 October 2015 / Accepted: 16 May 2016 / Published online: 21 May 2016

Abstract During summer, the intraseasonal disturbances over the Eastern Tibetan Plateau (ETP) can initiate development of severe weather system downstream. Previous studies yielded inconsistent results on the intraseasonal variability (ISV) of summer rainfall in terms of periodicity, genesis process and propagation pathway over the EPT based on small samples. In this study, we detected two dominant peaks of transient ISV, centered on quasi-biweekly (12–24) days (QBW) and quasi-9 (8–11) days using daily rainfall data over the ETP during the period of 1992–2012. Composite analysis revealed that the two ISVs were predominantly associated with the non-stationary wave trains, which traveled along different pathways. For the QBW, its mid-latitude wave train featured a upper-level southeastward migration, originating in Northern Europe and traveling via the East European Plain, the Ural Mountains, Lake Balkhash–Lake Baikal, the Mongolian Plateau, and then continued southward to the ETP and South Asia; and its tropical wave train was characterized with a northwestward/northward migration in low-level, starting from the Philippine Sea (PS)–South China Sea (SCS) region, moving over northern Bay of Bengal–SCS region, and arriving over the southern fridge of TP and southern China. In contrast, for quasi-9-day, the most significant mid-latitudes variability featured an eastward propagating upper-level wave train, originating from Western Europe, passing across the Mediterranean, the Black and Caspian seas, arriving over the TP, and moving towards East Asia; and the most evident tropical variability exhibited a clear northwestward/westward migration of a low-level wave train, originating from PS, passing over Taiwan, and subsequently moving towards southeastern China. Their different spatiotemporal features of associated wave trains caused their distinct linkages with eastern China rainfall anomalies. A "meridional pattern" with a giant Ural Mountain Ridge was the most remarkable precursory signals in upstream region before the QBW wet phase occurrence, which was different from the quasi-9-day. The major processes generating the local wet spells for the two modes were commonly linked to the preceding boundary warming, the upper-level negative vorticity and low-level prevalent winds, which triggered the ascending anomaly and lower tropospheric pre-moistening. We also discussed the co-variation of the wave trains between mid-latitudes and low-latitudes. The distinct evolution related with the two ISVs over the ETP described here may provide a useful guidance for 2–3 weeks (extended range) forecasts over the ETP and its downstream regions.

✉ Jing Yang
yangjing@bnu.edu.cn

[1] State Key Laboratory of Earth Surface Processes and Resource Ecology (ESPRE), Beijing Normal University, Beijing 100875, China

[2] State Key Laboratory of Numerical Modeling for Atmospheric Sciences and Geophysical Fluid Dynamics (LASG), IAP/CAS, Beijing, China

[3] Department of Atmospheric Sciences, and International Pacific Research Center, University of Hawaii at Manoa, Honolulu, HI 96825, USA

[4] Earth System Modeling Center, Nanjing University of Information Science and Technology, Nanjing 210044, China

1 Introduction

On the intraseasonal time scale, the anomalies of the vortex over the Tibetan Plateau (TP) can strongly affect the initiation and development of drought and flooding conditions in

the Asian monsoon region during the boreal summer (Tao and Ding 1981; Zhou et al. 2000; Ren et al. 2007; Dugam et al. 2009; Wang et al. 2009; Duan et al. 2012; Zhang et al. 2014). This linkage may be through downstream propagation (Liu et al. 2014; Yang et al. 2014) or by modifying the associated circulations (Fujinami and Yasunari 2004, 2009; Yasunari and Miwa 2006; Watanabe and Yamazaki 2012). Therefore, recognizing the intraseasonal variation (ISV) over the TP is crucial for improving extended range forecast of both local and downstream regions (Chou et al. 2010; Huang et al. 2011).

Previous studies dealt with a single case or a small sample of data based on limited number of years, and consequently failed to provide a consistent periodicity, behavior and genesis process of the ISV over TP during summer. In terms of the periodicity, a quasi-15-day period was found in the east–west oscillation of the South Asian High during summer 1981 (Liu and Liu 1991). Nitta (1983) showed 10–20 days and quasi-30-day oscillation in precipitation and relative vorticity over the Eastern Tibetan Plateau in 1979 (his Fig. 7). Endo et al. (1994) revealed quasi-15-day oscillation was dominated in meteorological elements in the central TP from the radiosonde data. Oscillations of 20–30 days, 14-day and nearly 8 days were identified in meteorological elements over the TP during summer 1998 (e.g., Yamada and Uyeda 2006; Zhang et al. 2014). Fujinami and Yasunari (2004) selected a 7–20 days filtered band to study convection activity over the TP in 1986, 1993 and 1998. Zhan and Li (2008) detected oscillations of 10–20 days and 30–60 days in upper-tropospheric water vapor during the summers of 2003 and 2004. Recently, Wang and Duan (2015) analyzed eight meteorological elements using 30 years datasets and also found the existence of three periodicities: 10–20-day period, 7–9-day and periods long than 30 days (see Fig. 1 of there work). In reference with the behaviors of TP ISV, inconsistent evolutions had been reported based on different cases, including a lower-level clockwise migration of convection anomalies around the TP (Fujinami and Yasunari 2004), eastward propagation across the TP (Zhan and Li 2008), southeastward propagation from Northern Europe, southward movement over the TP (Yang et al. 2014; Ren et al. 2015), northwestward propagation from western Pacific to Southeastern TP (Wang and Duan 2015), and remaining stationary over the TP (Zhan and Li 2008). Regarding the source of the ISV over the TP, one study found that it was caused by mid-latitude wave disturbances (Fujinami and Yasunari 2004); one study found its generation is associated with the tropical disturbances (Wang and Duan 2015); another assumed that it was generated by a local heating anomaly (Liu et al. 2007); and others considered that it was generated by remote heating such as the Indian Monsoon (Ding and Wang 2007). This lack of consensus highlights the need to further recognize and understand the ISV over the TP using long-term and continuously recorded datasets.

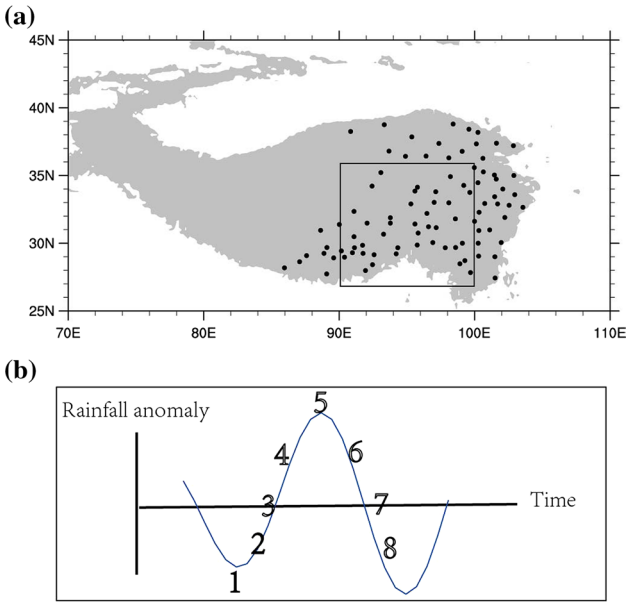

Fig. 1 **a** The geographical locations of the 90 CMA stations over the ETP, with the box denoting the core region of this study. **b** An example of the eight phases in one life cycle used in phase composite

Using 21-year (1992–2012) daily rainfall observations and daily reanalysis data at high spatial resolution, we attempted to recognize the the dominant periodicities, the types, their behaviors and discuss the mechanisms of ETP rainfall ISVs in this paper. We first introduced the datasets and methodology in Sect. 2, and then selected the dominant ISV periodicities and associated significant ISV events over the core region of the TP in summer in Sect. 3. In Sect. 4, the differences between two ISVs are demonstrated respectively in their spatial structures, evolutions, downstream rainfalls and large-scale circulation systems. The local genesis processes of the dominant ISV modes over the Eastern TP (ETP) are comprehensively depicted in Sect. 5. Section 6 summarized the distinct features of the dominant ISVs and discussed the possible linkage between the mid-latitudes and tropics.

2 Data and methodology

Since meteorological stations are very scarce over the western TP, we chose two types of precipitation datasets. One of them is the APHRODITE (Asian Precipitation–Highly-Resolved Observational Data Integration towards Evaluation of the Water Resources) gridded daily precipitation data, with a high resolution (0.5°) for the Asian monsoon region (60°E–150°E, 15°S–55°N) (Xie et al. 2007; Yatagai et al.

2012). This dataset was created primarily with measurements from a rain-gauge observation network, in operation from 1979 to 2007. The second dataset came from the China Meteorological Administration (CMA), which have 96 stations over the ETP (to the east of 90°E and above 2500 m), Among the 96 stations, four stations had no records after 1980, 12 stations began recording after 1992, and two stations began recording after 2000. Considering both the number and record length of these stations, we finally chose 90 stations with complete records from 1992 to 2012 (21 years) to investigate the ISV of ETP rainfall (Fig. 1a). The above two rainfall datasets produced similar results in our analysis. Considering the common record length, the following plots are mostly made from APHRODITE and CMA station data from 1992 to 2007. Since the APHRODITE data covered a larger area, the figures with spatial structures are mostly based on this dataset; the CMA station datasets show similar patterns. Because these two datasets only covered land, we also used the GPCP (Global Precipitation Climatology Project, Huffman et al. 2001) daily data starting from 1997 to verify our results, and they are consistent. The ERA-Interim data from the European Centre for Medium-Range Weather Forecasts (Simmons et al. 2007) at a resolution of 1.5° by 1.5° (http://data-portal.ecmwf.int/data/d/interim_daily/) was used to depict daily circulation changes. It also covers the 16 years from 1992 to 2007.

To identify the dominant ISV periodicities statistically, we first applied a fast Fourier transform (FFT) with a tapered window (Bingham et al. 1967), which is one of the most common methods of spectral analysis, to the time series to remove annual cycles at a given location for each summer (i.e., June–August) for the 21 years (1992–2012). We then calculated the average of each individual power spectrum for each summer. The statistical significance of each power spectrum was tested according to the method in Gilman et al. (1963), based on the power spectrum of mean red noise. The specific ISV component anomaly was extracted using a specific band filtering based on Fourier harmonic analysis of the intraseasonal component; the intraseasonal component was obtained from the raw daily precipitation time series by removing first the annual cycle and the synoptic fluctuations (for detail of the methodology, see Yang et al. 2010, 2014).

Phase composite analysis (detail provided in Sect. 3.2) was applied to specific variables to identify the spatial structure and temporal evolution of the ISV (Mao and Chan 2005). To perform a composite analysis of the significant ISV cases, we separated each cycle of the selected ISV events into eight phases (Fig. 1b). Phase 1 was the minimum (peak dry phase), and phase 5 was the maximum (peak wet phase). Phases 3 and 7 were the transitions from dry to wet phase and from wet to dry phase, respectively. Phases 2, 4, 6, and 8 occurred when the cycle reached half of its maximum or minimum value. Thus, the structure and evolution of each ISV mode was examined based on its life cycle following Yang et al. (2014).

We also carried out a lead–lag regression analysis to verify the results from the phase composite analysis. The lead–lag regression analysis of each meteorological field was conducted against the ISV-filtered rainfall, averaged over the core region at the peak wet phase. Given that the results of the composite analysis and regression analysis were similar, we only showed the results from the phase composite analysis. These composite anomalies are compared to the whole summertime series for significance estimation, using the Student's t-test and significance level of 90 %.

3 Dominant intraseasonal periodicities of summer rainfall over the ETP

3.1 Core region and peak season of intraseasonal summer rainfall over the ETP

Using the two rainfall datasets, we calculated the climatological mean state, the intraseasonal variance and the fractional variance of the intraseasonal signals for the rainfall over the TP during summer (Fig. 2a–c). The intraseasonal component was obtained from the raw daily precipitation time series by removing first the annual cycle and then the synoptic fluctuations using a 5-day running mean. Fractional variance is the ratio of intraseasonal variance against total rainfall variance. According to the magnitudes of the above three fields over the TP using the APHRODITE data (left in Fig. 2a–c) and the CMA station data (right in Fig. 2a–c), we selected the domain (90°–100°E, 27°–36°N) as the core region of TP summer rainfall. We can see a large seasonal mean, strong intraseasonal signals and a larger fractional variance of the ISV in this core region (the ETP hereafter). Note that the core region is different from other studies like Wang and Duan (2015).

Moreover, the time series of the area-averaged monthly-mean rainfall over the ETP (Figure ignored) indicated that the maximum rainfall there occurred in June, July and August (JJA), peaking in July. Therefore, the following analysis focused on the ETP and peak wet season (JJA).

3.2 Dominant intraseasonal summer rainfall periodicities over the ETP

To identify the dominant intraseasonal periodicities, we extract the dominant periodicities based on two strategies. Firstly, we made a 21-summer-averaged and a 16-summer-averaged power spectrum, respectively, of the area-averaged rainfall ISV components over the ETP using the two datasets (lines in Fig. 3a, b). Based on the 95 % confidence

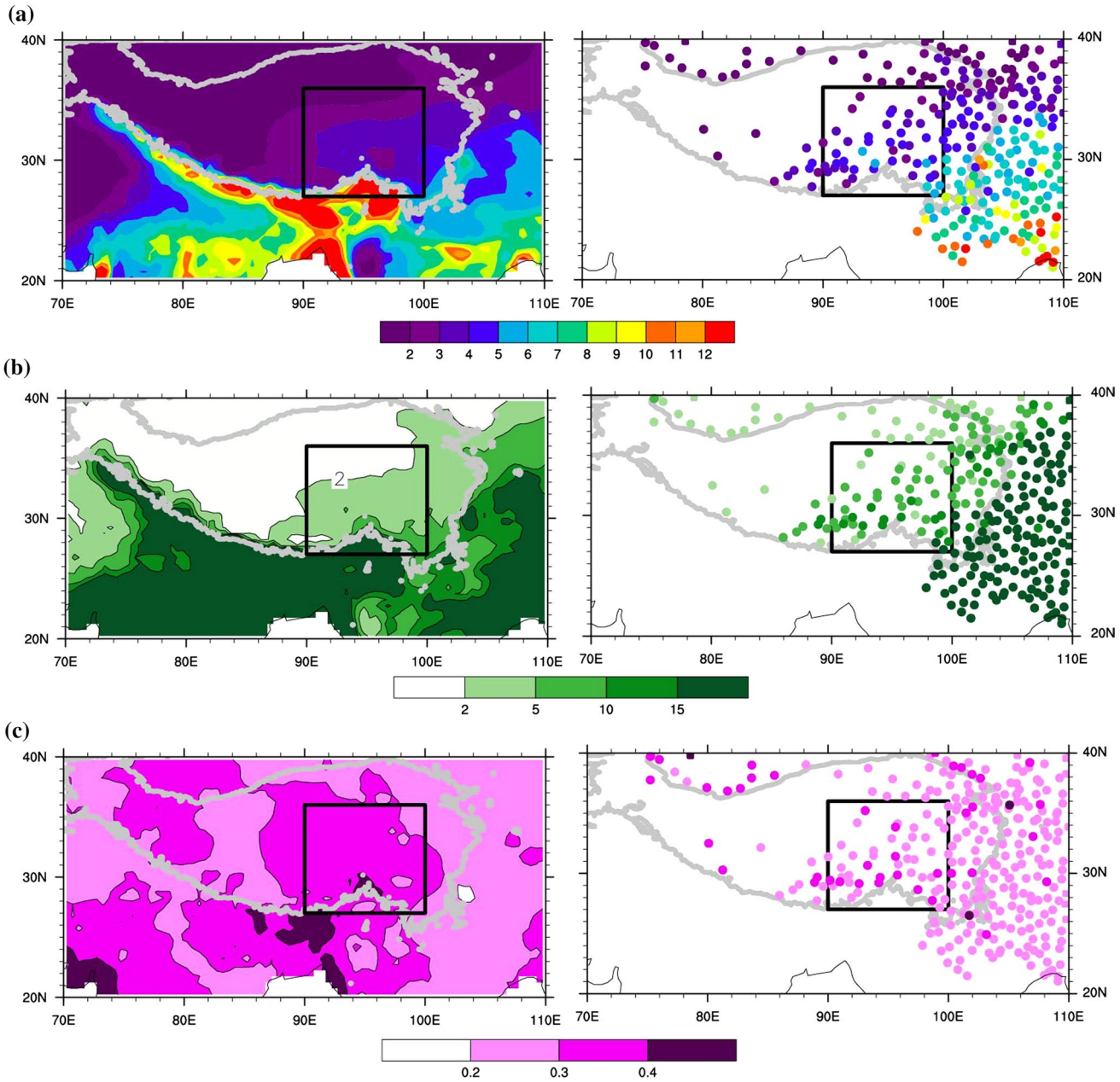

Fig. 2 **a** Climatological total rainfall during JJA (mm/day), **b** climatological intraseasonal variance of rainfall during JJA (mm^2/day^2), and **c** climatological intraseasonal fractional variance of rainfall during JJA (%). *Left panels* are from APHRODITE data, and *right panels* from CMA station data. Grey contour is 2500-m isoline. *Black box* is the selected domain over ETP

level, two bands were well identified over the ETP during JJA, over 12–24 and 8–11 days periods. Secondly, we made a power spectrum of each summer rainfall and then counted the total frequencies for each periodicity when its spectral power reached above 95 % confidence level (shading in Fig. 3a, b), and the results further confirmed the two intraseasonal bands were dominant ISV signals of summer rainfall over the ETP. Hence, both multi-year averaged and year-by-year power spectral analyses indicated that the 12–24 days and 8–11 days bands were two major ISV components of summer rainfall over the ETP, and the 12–24-day was the most dominant ISV component. In addition, we also checked the multi-year averaged power spectrum for other meteorological fields (i.e., surface air temperature, surface heating flux, vorticities et al.), which also markedly exhibited the above two intraseasonal peaks in summer (Figures ignored here). These two ISV modes were also shown in the Fig. 1 of Wang and Duan (2015) although their work focused on a bigger area of TP and only studied the 10–20-day period. Our study intends to

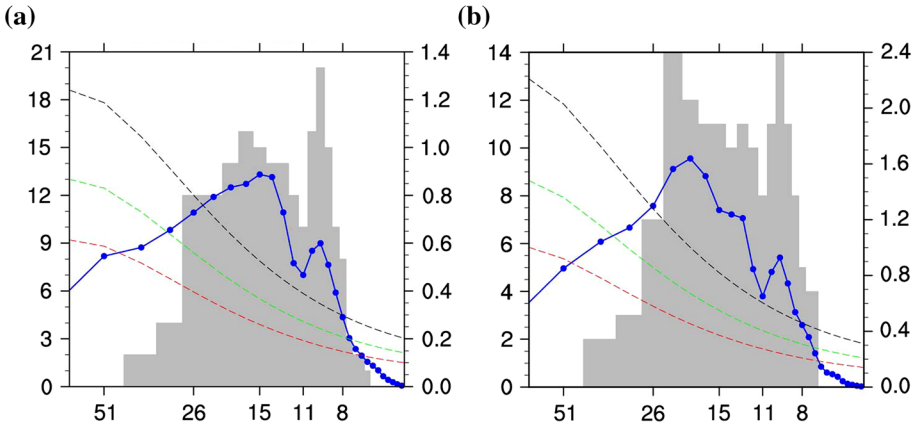

Fig. 3 **a** The 16 summer-mean (JJA-mean) power spectra of the rainfall ISV component over the ETP according to the CMA station data (*blue line* and *right y* axis) and the frequencies for each periodicity when its spectral power reached above 99 % confidence level (*shading* and *left y* axis); the Markov *red* noise spectrum is shown by a *red dashed line*, the priori 99 % confidence level is marked by the *green dashed line*, and the posteriori 99 % confidence level by a *black dashed line*. The *x*-axis has been rescaled using the natural logarithm of frequency, and the corresponding *y*-axis is multiplied by frequency. **b** The same as (**a**), except for APHRODITE data

distinguish the differences of the two ISV modes so that a parallel analysis will be made for them. For brevity, we called these two ISV modes as quasi-biweekly (QBW) (12–24 days) and quasi-9-day (8–11 days) modes hereafter.

3.3 Selection of significant intraseasonal summer rainfall events over the ETP

Phase composite analysis required that the significant events of the two ISV modes be chosen. The area-averaged daily time series of both unfiltered rainfall and ISV-filtered rainfall over the ETP were presented year by year in Fig. 4. Two major criteria were used to select the significant ISV events: (1) both the maximum amplitude in the wet phase and one of the minimum amplitudes in the dry phase exceeded 0.8 standard deviations of the time series of the area-averaged band-filtered rainfall; and (2) one wet peak and two dry peaks in the selected ISV event from the time series of the band-filtered rainfall were well identified in the time series of total rainfall. According to the two criteria, 35 significant QBW cycles and 47 significant quasi-9-day cycles were selected from 16 summers.

Note that a period longer than 30 days can be also seen in some summer time series (e.g., 1995, 1999) but not significantly shown in averaged spectrum results. And we also noticed that this period longer than 30 days was usually fixed in early summer. Therefore, we speculated that this longer periodicity essentially could belonged to a portion of climatological ISO (CISO, Wang and Xu 1997). To clarify this assumption, we made a climatological daily mean (after removing synoptic scale and annual cycle) of 16-year summer rainfall averaged over the ETP region shown as in Fig. 5a, and found that this longer period (quasi-40 days) was the most significant periodicity of CISO over ETP (Fig. 5a). This quasi-40-day CISO cycle was phase-locked in the period from mid-June to mid-to-late July, which was just consistent with the second cycle of CISO (Western North Pacific (WNP) monsoon onset) mentioned in Wang and Xu (1997). Accordingly, the corresponding evolutions of the atmospheric circulations were demonstrated in Fig. 5b. From the mid-June to the early July, the western North Pacific Subtropical High (WNPSH) experienced a northward jump; and then retreated eastward from early July to late July. Therefore, the quasi-40-day was considered to be the major periodicity of the rainfall CISO over ETP, which was just in agreement with WNP monsoon subseasonal march. Rather than CISO, the following study focused on those cases associated with two dominant transient ISV modes over ETP (QBW and quasi-9-day).

4 Distinguishing the two rainfall ISVs over ETP

Eight-phase composite analysis was applied to the two intraseasonal (QBW and quasi-9-day) band-filtered fields for the selected significant events. We aimed to investigate the transient spatial structures and evolutions, rainfall and large-scale circulations associated with the two rainfall ISVs. In the following descriptions, the spatial structures, rainfall and large-scale circulations focused on peak phases (P1 and P5, i.e., extreme dry and wet); the evolutions focused on the first half-life cycle from phases 1 to 5 (from extreme dry to extreme wet), because the next half cycle from phases 5 to 8 is nearly a mirror image of the first half-life cycle, which can be also considered as the previous half-life cycle prior to the first half-cycle.

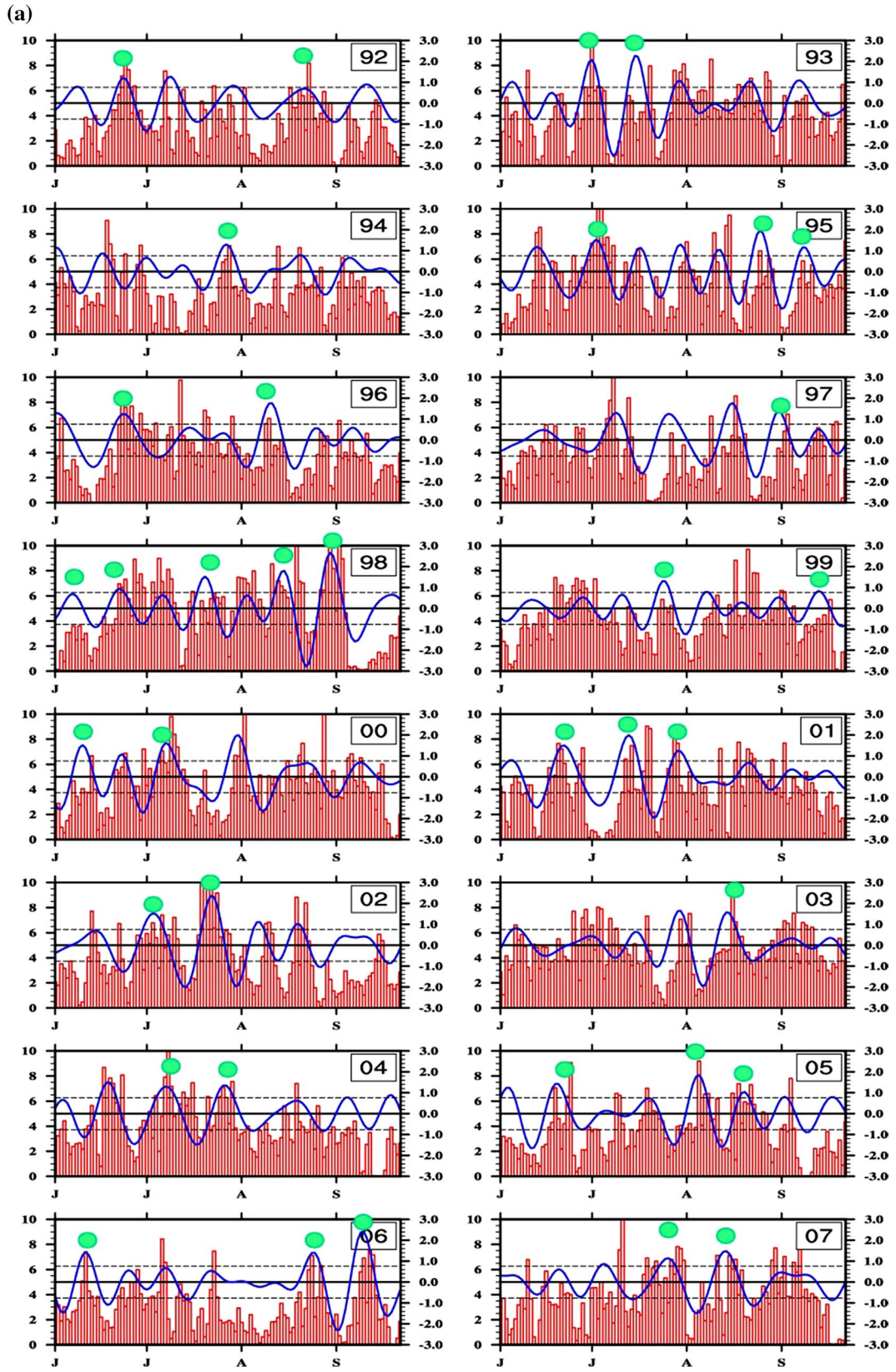

Fig. 4 Time series of **a** QBW and **b** quasi-9-day filtered rainfall (*blue curves*). The left *y*-axis is unfiltered rainfall (*red bars*), and the right *y*-axis is filtered rainfall averaged over the core region during each summer. The *green dots* denote the selected significant cases of the two modes according to the given criteria; and the *dashed line* represents one standard deviation. *Unit* mm/day

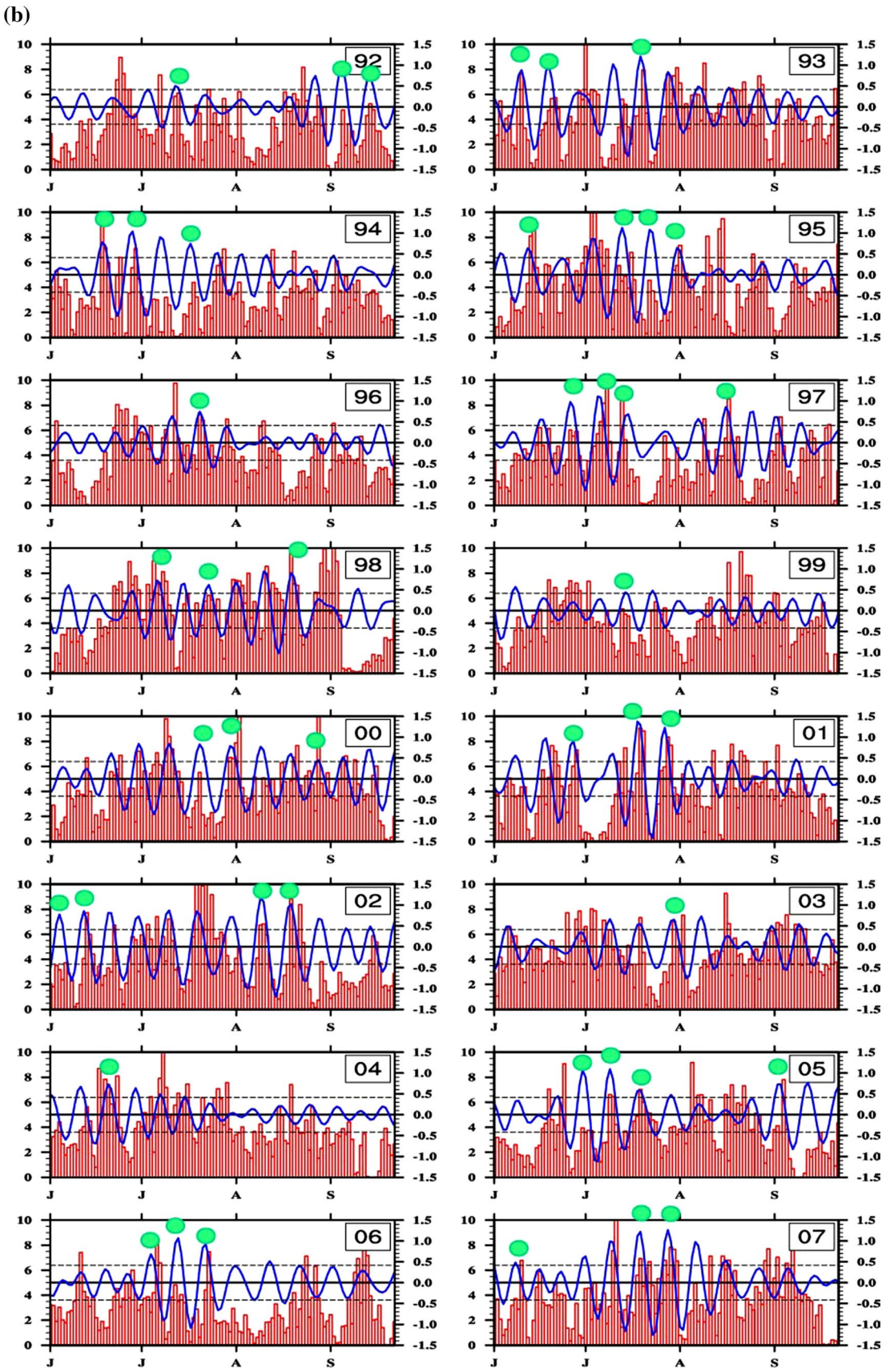

Fig. 4 continued

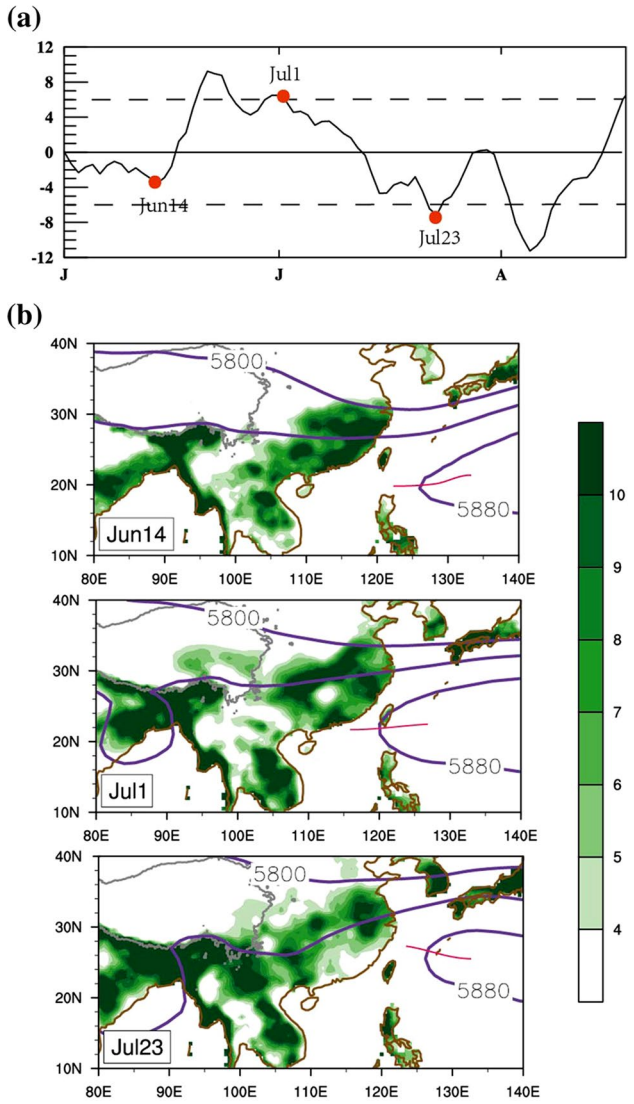

Fig. 5 **a** Time series of climatological ISV for the rainfall averaged over the core region of ETP (mm/day), **b** the climatological mean rainfall (*shading* mm/day) and 500-hPa geopotential height (*purple line* m) associated with climatological ISV key date. The *red lines* denote the rough position of WNPSH ridge

4.1 Distinct transient atmospheric circulation patterns associated with the two types of ISVs at their extreme phases

Shown as in Fig. 6, we presented the three-dimensional structures of transient atmospheric circulation in the extreme dry phase of ETP rainfall as an example, respectively using 200, 500 and 850 hPa to represent upper-, mid- and lower-troposphere. And the extreme wet phase was a mirror image of the extreme dry phase. In the upstream region (west and north) of ETP (high-latitudes) (left panel of Fig. 6a, b), the most significant feature of atmospheric circulation for either ISV was a well-developed transient wave train with a quasi-barotropical structure with a slight westward tilt from low- to upper-levels. However, two types of wave trains related with the two ISVs had different spatial patterns. At the QBW extreme phase, the transient wave train extended in a northwest-southeast direction, and the major transient centers were respectively positioned over Northern Europe, the Ural Mountains, Lake Balkhash–Lake Baikal, and Mongolian Plateau-northern China, ETP, and southern fridge of TP (left panel of Fig. 6a, b). And the upper-level transient vorticities elongated in an east–west direction and featured a north–south contrasting pattern along TP longitudes. By comparison, at the quasi-9-day extreme phase, the wave train obviously extended in an east-west direction almost along the upper-level westerly jet (right panel of Fig. 6a, b). And its transient maximum centers at extreme phase are respectively located over Western Europe, Black sea, Caspian seas and Lake Balkhash, northwestern TP and southeastern TP-southern China (right panel of Fig. 6a, b). And its upper-level transient vorticity primarily elongated in a northeast–southwest direction.

In the downstream region (east and south) of TP (low-latitudes), the similar characteristics for both ISV modes was that the easterly/northeasterly anomalies were observed in low-troposphere over the southern fridge of TP at extreme dry phase and the westerly/southwesterly anomalies prevailed over southern fridge of TP at extreme wet phase (Fig. 6c). However, we can clearly detect their distinguishable differences in the low-level troposphere (Fig. 6c). For QBW, the most striking anomaly is an east-west extended cyclonic (anticyclonic) anomaly that spanned over the whole South Asian region covering northern Arabian Sea, northern Bay of Bengal (BoB) and northern South China Sea (SCS) regions at extreme dry (wet) phase (left panel of Fig. 6c). Meanwhile, a giant low-level anticyclonic (cyclonic) anomaly appeared over East Asia; In contrast, for quasi-9-day mode, a distinguishable low-level southeast-northwest tilted wave train was observed from tropical WP to eastern China, and the maximum centers of this wave train were respectively positioned over tropical western Pacific, Philippine Sea (PS), East China Sea, and southeastern China (right panel of Fig. 6c).

4.2 Distinct atmospheric circulation evolutions associated with two types of ISVs

4.2.1 QBW

In mid-latitudes, the most significant feature related with the QBW oscillation of ETP rainfall was a non-stationary wave train over the Eurasian continent as mentioned in the previous section. As Fig. 7 showed, the wave train started over Northern Europe, and passed over the East European

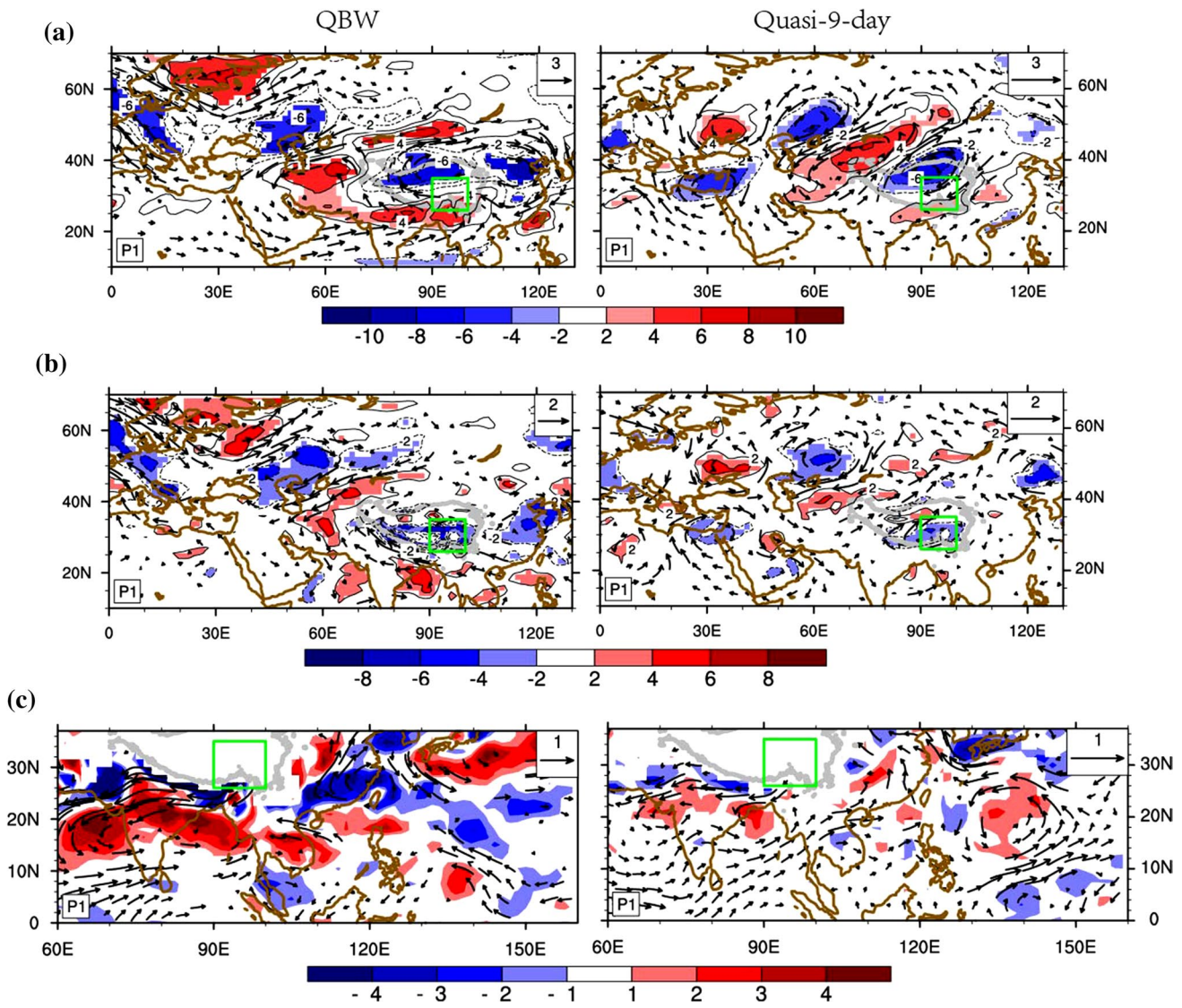

Fig. 6 **a** 200-hPa vorticity (10^{-5}/s) and winds (m/s), **b** 500 hPa vorticity (10^{-5}/s) and winds (m/s), **c** 850 hPa vorticity (10^{-5}/s) and winds (*vector* m/s) respectively in the QBW anomaly (*left panel*) and quasi-9-day anomaly (*right panel*) at extreme dry phase (*Phase 1* P1). *Shadings* and *vectors* are above 90 % significant level. The *green box* is the core domain and the *grey* contour is 2500 m isoline

Plain, the Ural Mountains, Lake Balkhash–Lake Baikal region, and finally arrived over the Mongolian Plateau-northern China. After having passed over the TP, it moved towards South Asia. This wave train exhibited a typical barotropical structure (as mentioned above) and propagated southeastward before reaching the TP. When the wave train arrived above the Mongolian Plateau, it began to propagate southward along the South Asia high steering flow and climbed above the TP. After climbing above TP, the transient anomaly turned into a baroclinic structure (as mentioned above).

In low latitudes, the most noticeable feature of the circulation anomalies for this time scale was located south of the TP, which exhibited a northwestward/westward migration of the low-level circulation from western Pacific via southern fridge of TP to Arabian Sea (Fig. 8). At P2, a significant band of positive anomalous vorticities (anticyclonic anomaly) appeared around 10°N, striding over PS-SCS region (Fig. 8); then the anomalous band obviously extended westward and migrated northwestward. Around 6–7 days later at P5, it moved to the latitudes around 20°N, spanning over northern Arabian Sea-northern BoB–SCS region at ETP extreme wet phase. Afterwards, it continuously migrated westward and reaches over Arabian Sea. The westward migration of quasi-biweekly oscillation nearly along 10–20°N has been reported in many previous

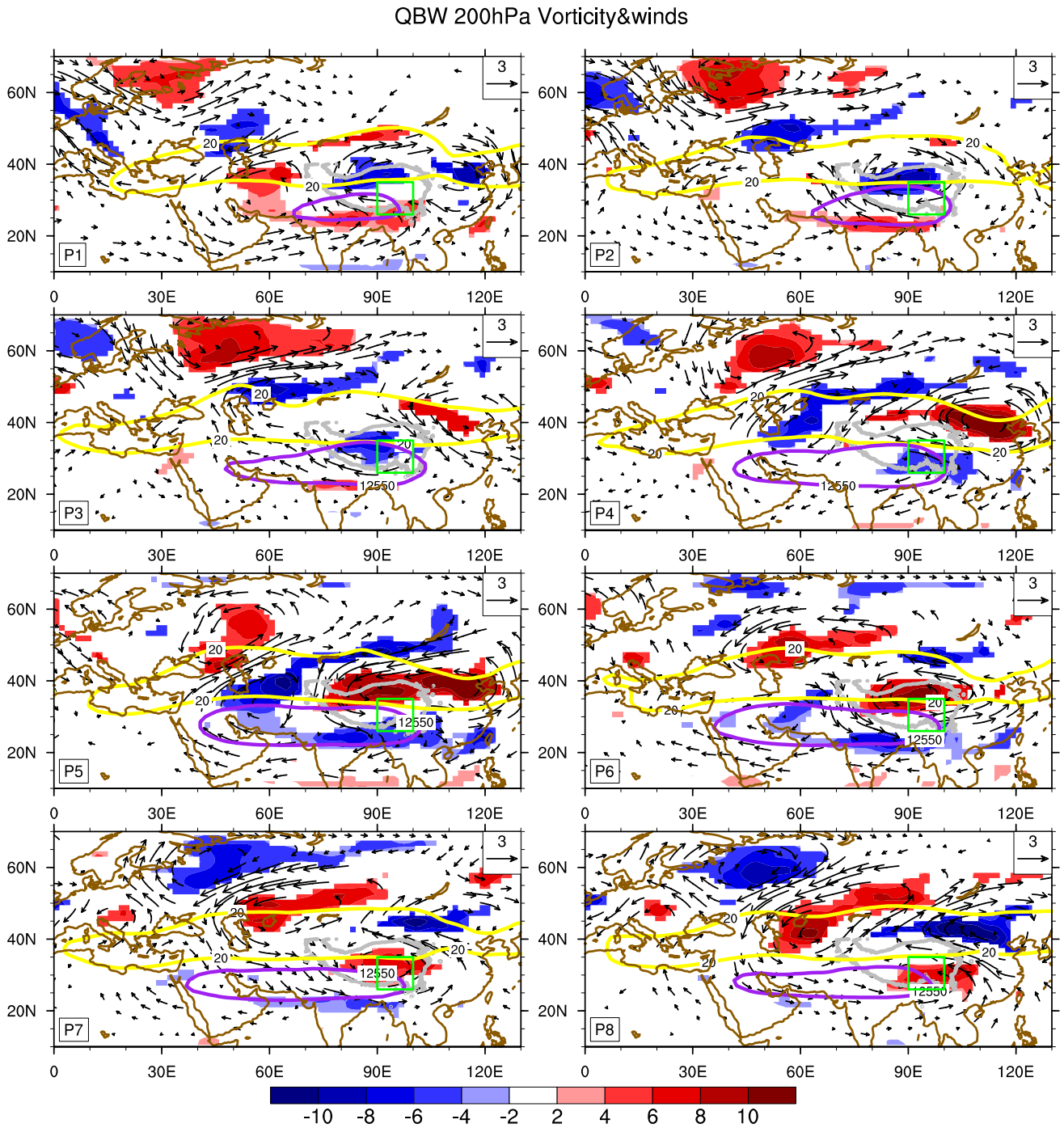

Fig. 7 Temporal evolution of 200-hPa vorticities (10^{-5}/s) and winds (m/s) in the QBW day anomaly based on the eight phase composite in JJA. *Shadings* indicate regions with 200-hPa vorticities at or above the 90 % confidence level. *Yellow line* is a 200-hPa zonal wind contour with 20 m/s that roughly denotes the location of westerly jet. *Purple line* is a 200-hPa geopotential height contour with 12,550 m that roughly represents the SAH location. The *green box* is the core domain and the *grey* contour is 2500 m isoline

studies (e.g., Annamalai and Slingo 2001; Chen and Chen 1995; Yang et al. 2008). In short, the transient circulations associated with QBW mainly featured a co-variation with a southeastward migration from mid-latitudes as well as a northwestward migration from low-latitudes.

4.2.2 *Quasi-9-day*

In mid-latitudes, the most striking signal with the quasi-9-day mode was a wave train extending in an east-west direction (Fig. 9). In contrast to the QBW, the wave propagation

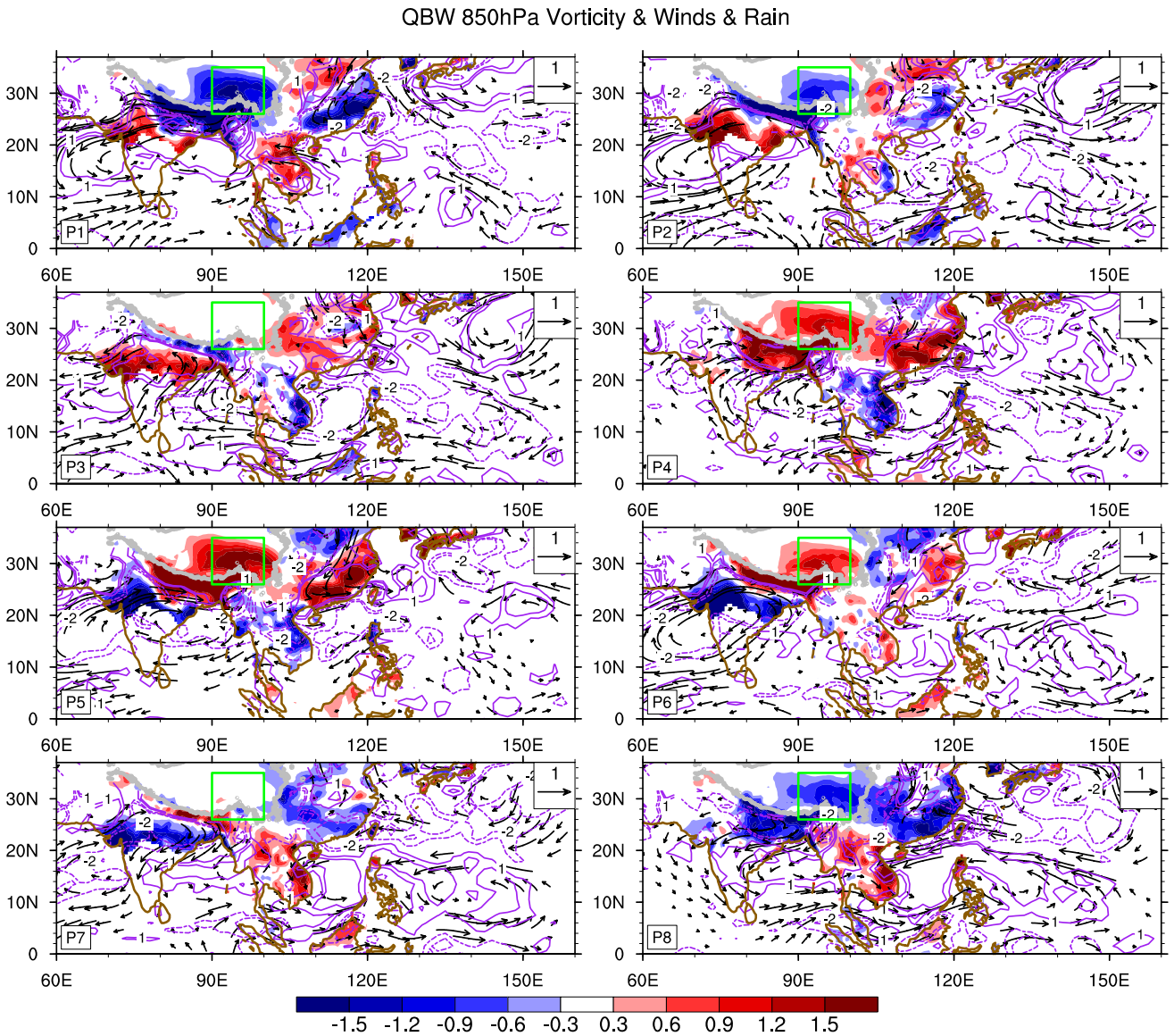

Fig. 8 Temporal evolution of 850-hPa vorticity (*contour* 10^{-5}/s), 850-hPa winds (*vector* m/s) and rainfall (*shading* mm/day) in the QBW day anomaly based on the eight-phase composite in JJA (above the 90 % significance level). *Solid* and *dashed lines* denote the positive and negative vorticity anomaly, respectively. The *green box* is the core domain and the *grey* contour is 2500 m isoline

followed an eastward direction roughly along the westerly jet. This wave train originated from Western Europe, passed across the Mediterranean, Black and Caspian seas, arrived at the TP, and moved towards East Asia (Fig. 9). Similar to the QBW, this wave train had a barotropical structure before reaching the TP, but became a typical baroclinic feature over the ETP.

In low latitudes, the most distinguishable anomalies were a low-level wave train extending in a northwest-southeast direction from tropical western Pacific to southwestern China as shown in Fig. 10. A clear northwestward migration of this wave train was seen originating from tropical western Pacific, going through PS, passing over Taiwan, and moving towards eastern China and central eastern China. Therefore, the quasi-9-day mode was mainly characterized by a co-variation with an eastward propagation in mid-latitudes and northwestward propagation in low-latitudes, which was obviously different from QBW.

4.3 Distinct rainfall patterns over eastern China associated with the two ETP ISVs at their extreme phases

The rainfall anomalies were mainly determined by the anomalous low-level circulation and water-vapor

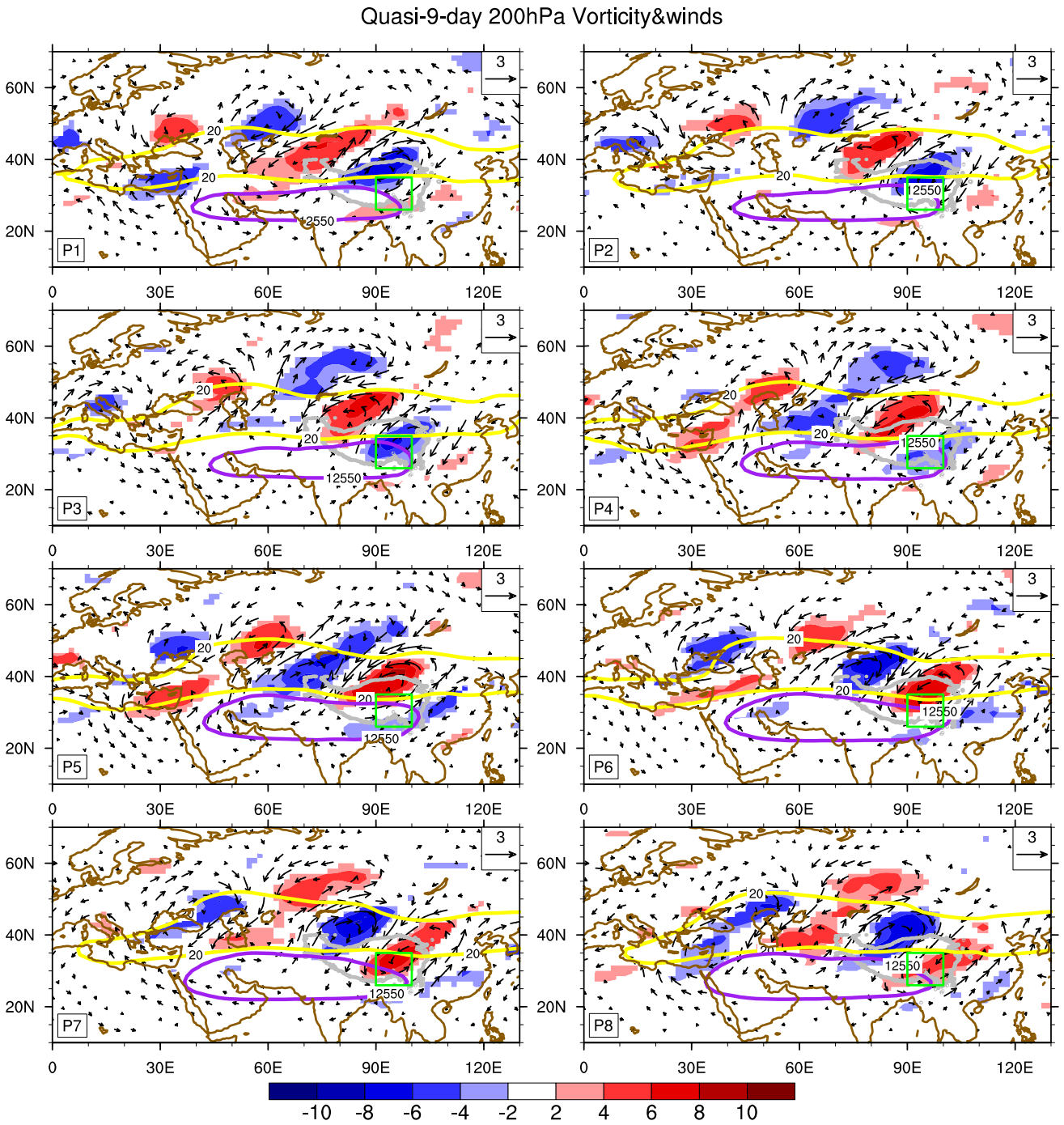

Fig. 9 Temporal evolution of 200-hPa vorticities (10^{-5}/s) and winds (m/s) in the quasi-9-day anomaly based on the eight phase composite in JJA. *Shadings* indicate regions with 200-hPa vorticities at or above the 90 % confidence level. *Yellow line* is a zonal wind contour by 20 m/s that roughly denotes the location of westerly jet. *Purple line* is a 200-hPa geopotential height contour by the 12,550 m that roughly represents the SAH location. The *green box* is the core domain and the *grey* contour is 2500 m isoline

transportation. Because the two ISVs had different spatial patterns and evolutions of atmospheric circulations, the associated downstream rainfall patterns over eastern China were different. Since the QBW was characterized by north–south meridional contrasting patterns along the TP latitudes and the transient vortex featured an evident east–west extension (Figs. 7, 8), there was a significant cyclonic anomaly in the lower level over the Southeast China–East China Sea region at the extreme wet phase over ETP (Fig. 8). As a result, the southeastern China suffered a

wet phase accompanying the wet phase over the ETP (P5 of Fig. 8).

In contrast, the anomalies of the quasi-9-day mode featured east-west zonal contrasting patterns (Figs. 9, 10). The downstream region of TP featured a westward/northwestward migratory wave from western Pacific (Fig. 9). At the extreme wet phase over ETP, two low-level cyclonic anomalies were positioned respectively over the Sichuan Basin and the coastal southeastern China, and a low-level anticyclonic anomaly was located over the central-South China (Fig. 10). Therefore, the Sichuan Basin was wet while the central-South China was dry when the rainfall anomaly was positive over the ETP (P5 of Fig. 10).

From the perspective of sub-seasonal prediction of rainfall in the downstream region, if we take the ETP rainfall anomaly as a precursor for the southeastern China. these two ISVs could have different hints. In the case of the QBW intraseasonal event, the coastal southeastern China tends to suffer a wet phase after 6–9 days of the dry phase over the ETP (Fig. 8). In contrast, a dry phase could appear over the Central-South China 3–5 days after the dry phase over the ETP for the quasi-9 day ISV mode (Fig. 10).

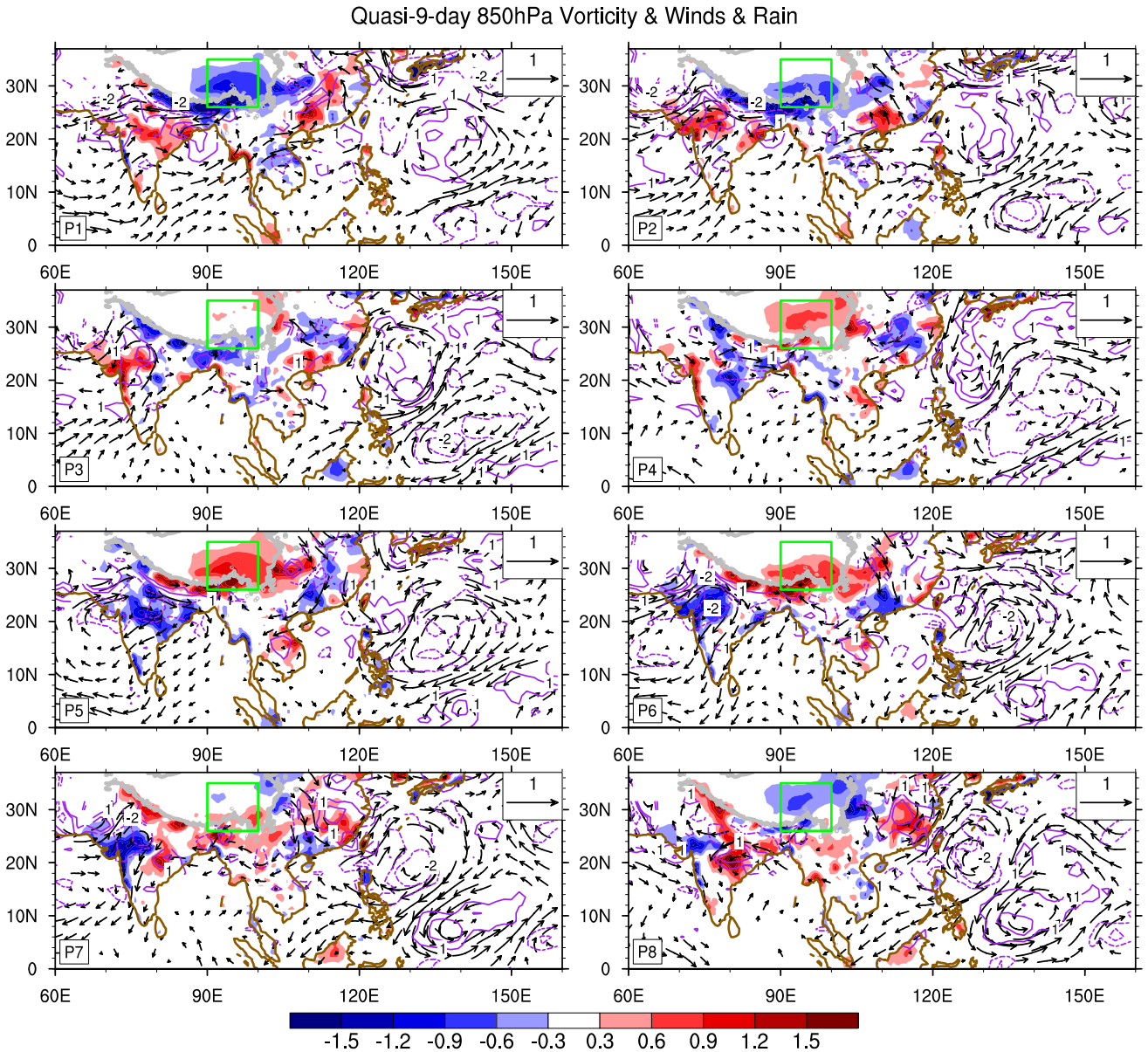

Fig. 10 Temporal evolution of 850-hPa vorticity (*contour* 10^{-5}/s), 850-hPa winds (*vector* m/s) and rainfall (*shading* mm/day) in the quasi-9-day anomaly based on the eight-phase composite in JJA (above the 90 % significance level). *Solid* and *dashed lines* denote the positive and negative vorticity anomaly, respectively. The *green box* is the core domain and the *grey* contour is 2500 m isoline

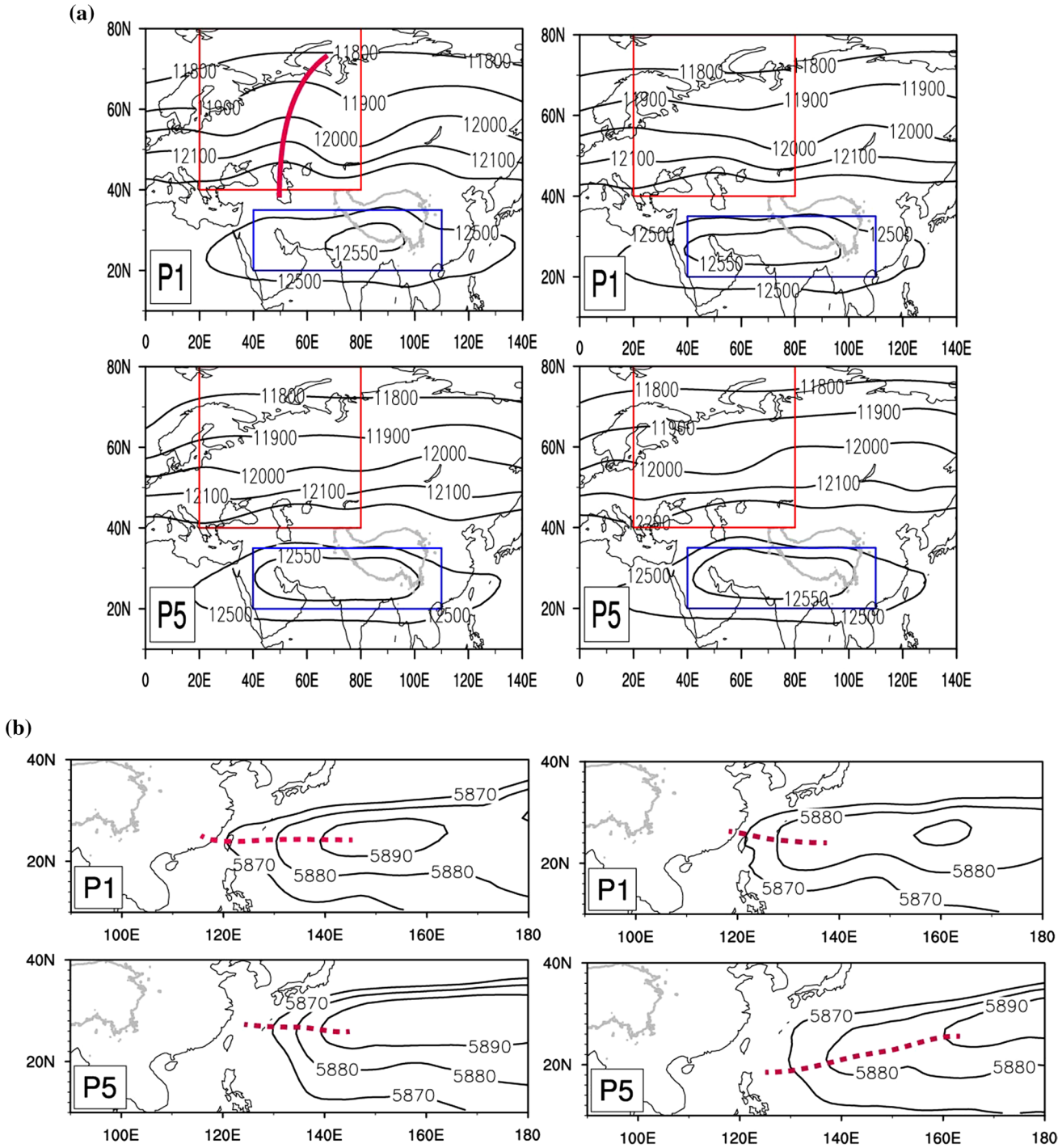

Fig. 11 Composites of total geopotential height during phase 1 (extreme dry phase) and phase 5 (extreme wet phase) at **a** 200 hPa and **b** 500 hPa for the QBW day mode (*left*) and quasi-9-day mode (*right*), respectively. *Units* 10^2 m^2/s^2. The *red* and *blue boxes* respectively *highlight* the Ural Mountain Ridge location and South Asian High; the *red dashed line* roughly denotes the WNPSH ridge

4.4 Distinct large-scale circulation patterns associated with the two ETP ISVs

The intraseasonal transient perturbations could modify the large-scale atmospheric circulation. As Fig. 11a showed, the mid-latitude atmospheric circulation associated with the QBW were characterized with a "meridional pattern" with a giant Ural Mountain Ridge and a giant Lake Balkhash trough at the extreme dry phase (left panel in Fig. 11a). With the southeastward propagation of the transient

perturbation from extreme dry to extreme wet phases, the Ural Mountain Ridge disappeared and meridional pattern changed to a quasi-zonal pattern. Compared with the QBW mode, the mid-latitude atmospheric circulation related with quasi-9-day exhibited a "zonal pattern" at the extreme dry phase (right panel in Fig. 11a), without strong ridges and troughs in the upstream regions of TP. Therefore, that there is a "meridional pattern" with a giant Ural Mountain Ridge or not is considered to be the most striking precursory signal to distinguish the upstream large-scale circulations of two ISVs before their extreme wet phase.

We also examined two important circulation systems: South Asia High (SAH) and WNPSH. They have different behaviors in the two intraseasonal time scales. During the transition from the dry to the wet phase, the SAH was evidently enhanced with markedly eastward and westward extension (left panel in Fig. 11a). Simultaneously, the WNPSH exhibited a remarkable northeastward displacement (left panel in Fig. 11b). In comparison, During the transition from the dry to the wet phase, the SAH exhibited slightly eastward extension (right panel in Fig. 11a), while WNPSH only retreat eastward without northward shift (right panel in Fig. 11b).

5 Local rainfall genesis related with two ISVs over ETP

The previous two subsections objectively described the distinct features of atmosphere circulation associated with two types of rainfall ISV modes over ETP, including structures, evolution and large-scale circulations. This subsection would investigate how the local (ETP) peak wet phase was generated. In order to clarify this question, we examined the spatiotemporal evolutions of different thermo-dynamical fields over the core domain, focusing on the transition from the extreme dry to the extreme wet for both ISV modes.

According to Fig. 12, we noticed that the major features associated with local rainfall generation were very similar between two ISV modes. First, ascending motion is the requisite condition for rainfall generation. During the transition from dry to wet phases, we noticed that the ascent anomaly had already appeared at P3 around two phases prior to the extreme wet phase, and was strengthened from P3 to P5 (Fig. 12a). Accompanied with the ascent anomaly, the anomalous divergence and convergence occurred respectively in the upper- and low-levels at the same time (Fig. 12b), and then the baroclinic structure was developed. Simultaneously, the low-level positive vorticity was also developed (Fig. 12c). Second, moisture supply is the other necessary condition for precipitation occurrence. Two phases prior to the extreme wet phase, we noticed the low-level positive specific humidity anomaly had already appeared over the lower troposphere to the southeast TP as well as over the southeastern TP at P3 (Figs. 12d, 13a, b). In this condition, the ascending motion could pump the moisture above the TP from southeast of TP, and then transport the moisture up to the mid-troposphere from the lower troposphere over southeastern TP (Fig. 12d). And the water vapor condensed into clouds and raindrops over the ETP and then released latent heat in the mid-troposphere (Fig. 12d). The maximum latent heating in the mid-troposphere in turn strengthened the ascending motion and enhanced the atmospheric baroclinic structure. Afterwards, the maximum rainfall anomaly was generated finally at extreme wet phase.

What caused the occurrence of both the ascent anomaly before the peak wet phase? To investigate this question, we first clarified what happened prior to the ascending motion. On one hand, an evident low-level warming appeared over ETP prior to the ascending motion (Fig. 12e). This warming just corresponded to the previous dry phase. The dry phase means the clear sky that indicates strong descent anomaly and increased downward solar radiation, which resulted in the low-level warming over ETP. Theoretically, the local warming breaks the geostropic balance between the air column thickness and the circulation, and then causes the lifting of the local atmosphere. The lifting could offset the warming through its associated adiabatic cooling (e.g., Ren and Wu 2003). On the other hand, the upper-level negative vorticity appeared prior to the ascent anomaly (Fig. 12a, c). This upper-level negative vorticity actually belonged to a northeastward/eastward propagating quasi-barotropical wavetrain from mid-latitudes associated with the QBW and quasi-9 day modes as mentioned in Sect. 4.2.

What caused the lower tropospheric pre-moistening over southeastern TP before the peak wet phase? For QBW, with the westward extension of the low-level anticyclonic anomaly from western Pacific region to South Asian region, the prevalent anomalous winds changed from northeasterly to southwesterly anomalies (starting from P3, Fig. 8) that could transport plenty of water vapor to southeastern fridge of TP and moistened the low-troposphere (Fig. 13a). In contrast, for quasi-9-day mode, with the northwestward propagation of the low-level transient disturbances from western Pacific region to eastern China, an anomalous cyclonic appeared over eastern China at P3. The according easterly and southeasterly wind anomalies became significant to east of TP and could transport moisture to southeastern fridge of TP and moistened the lower tropospheric atmosphere (Figs. 10, 13b). Therefore, the lower tropospheric pre-moistening conditions are caused by low-level water vapor transport that is directly related with low-level transient wave propagation from lower latitudes.

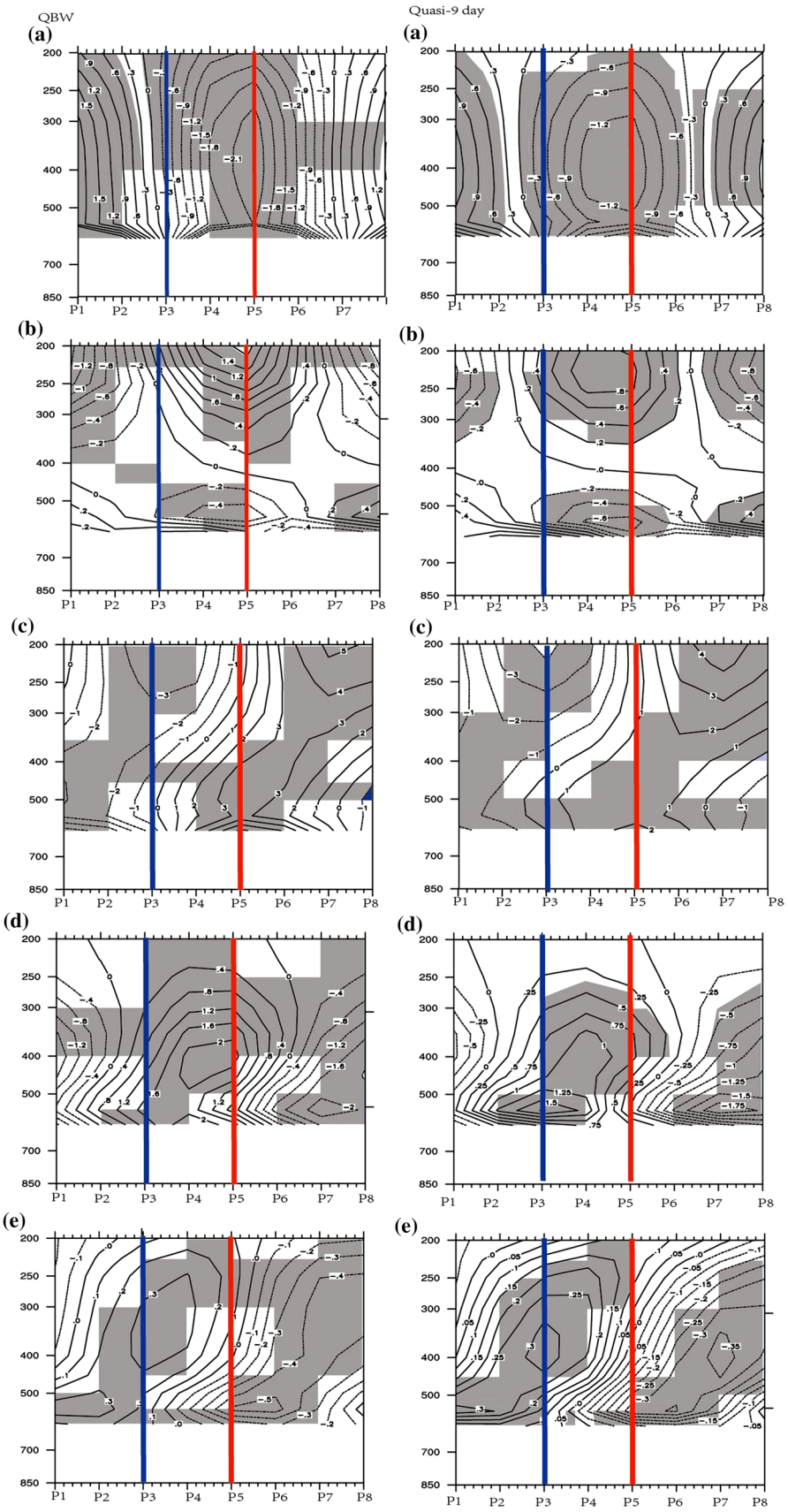

Fig. 12 Phase (*x*-axis)-pressure (*y*-axis hPa) diagrams in the core region of the composite values of the QBW filtered **a** vertical velocity (10^{-2} Pa/s), **b** divergence (10^{-5}/s), **c** vorticity (10^{-5}/s), **d** specific humidity (10^{-4} kg/kg), **e** Temperature (K) for the QBW mode (*upper panel*) and the quasi-9-day mode (*low panel*). *Red line* is peak wet phase and *blue line highlights* the timing that upward motion begins to occur

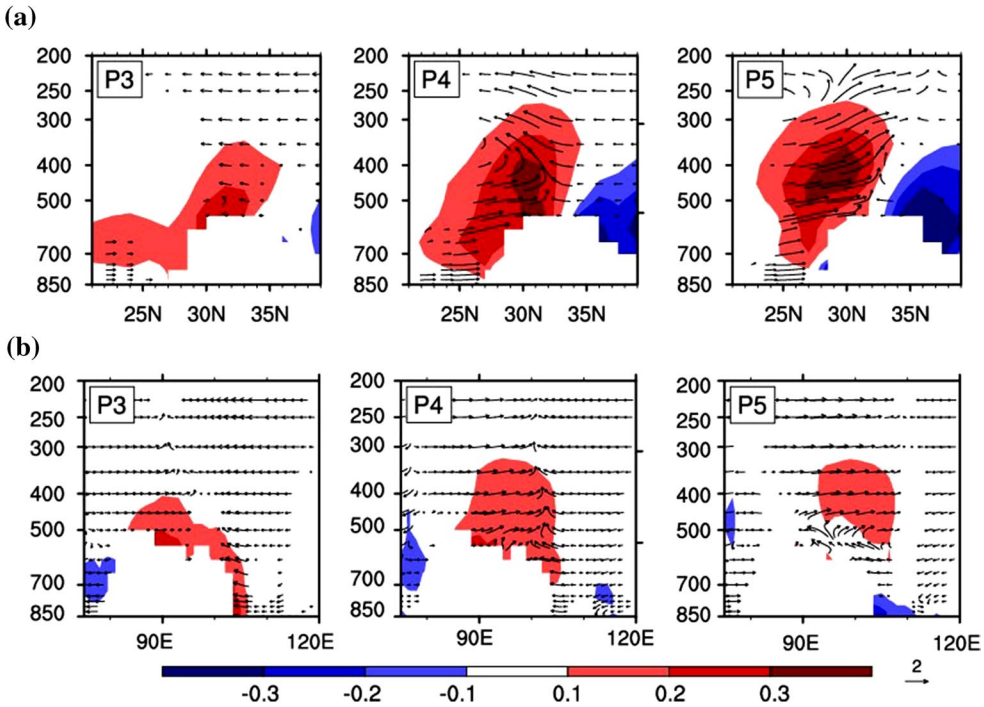

Fig. 13 **a** Latitude-pressure diagram of winds (*meridional velocity* m/s, *velocity* 10^{-2} Pa/s) and specific humidity (*shading* 10^{-4} kg/kg) averaged between 90–100°E for QBW, **b** longitude-pressure diagram of winds (*meridional velocity* m/s, *velocity velocity* 10–2 Pa/s) and specific humidity (*shading* 10–4 kg/kg) averaged between 27–36°N for quasi-9-day composite of anomaly. Above the 90 % significance level is shown

When the dynamical anticyclone arrived over ETP, the above-mentioned effect of local pre-warming and pre-moistening worked on it so that the baroclinic structure was well developed. Consequently, the dynamical anticyclone changed to a thermal anticyclone with an upper-level divergence and a low-level convergence, which induced the occurrence of extreme wet phase.

6 Summary and discussion

6.1 Summary

Based on rainfall datasets for 1992–2012, two significant intraseasonal periodicities were identified in the summer rainfall over the ETP, which were respectively 8–11 (quasi-9) and 12–24 (quasi-biweekly) days long, and accounted for more than 30 % of the variance of total rainfall. The two leading ISV modes over ETP have obvious different spatial patterns and evolutions although their periodicities are close to each other.

For QBW, a southeastward/southward upper-level migratory wave train was the most remarkable signal in mid-latitudes, which started over Northern Europe, passed over the East European Plain, the Ural Mountains, the Lake Balkhash–Lake Baikal region and the Mongolian Plateau, and subsequently passed over the TP and moved towards South Asia. In tropics, a northwestward/northward migration occurred at the same timescale, starting from the PS–SCS region, moving over northern BoB–SCS region, and arriving over the southern fridge of TP and southern China. These two propagating perturbations encountered over the southeast of TP. In contrast, for quasi-9-day, the most significant mid-latitudes variability featured an eastward propagating upper-level wave train, originating from Western Europe, passing across the Mediterranean, the Black and Caspian seas, arriving over the TP, and moving towards East Asia. At the same timescale, the tropical variability exhibited a clear northwestward/westward propagation of a low-level wave train, originating from PS, passing over Taiwan, and subsequently moving towards southeastern China and the Sichuan Basin. These two wave trains encountered each other over the eastern fridge of TP. Their different spatiotemporal features caused their distinct linkages with eastern China rainfall anomaly. And we summarized the above processes as shown in a schematic diagram (Fig. 14).

A "meridional pattern" with a giant Ural Mountain Ridge and a giant Lake Balkhash trough were found to be the most remarkable precursory signals in upstream region of TP before the QBW wet phase occurrence. In contrast, the quasi-9 day featured a "zonal pattern" mode in its high-latitude circulation fields. Additionally, two important circulations systems, SAH and WNPSH, also exhibited different behaviors associated with the two intraseasonal oscillation.

However, the major processes that generated the local wet phases over the ETP were similar between the two ISV modes, which are ascending motion and pre-moistening. Once the ascending motion appeared, the process with the positive feedback that generated precipitation

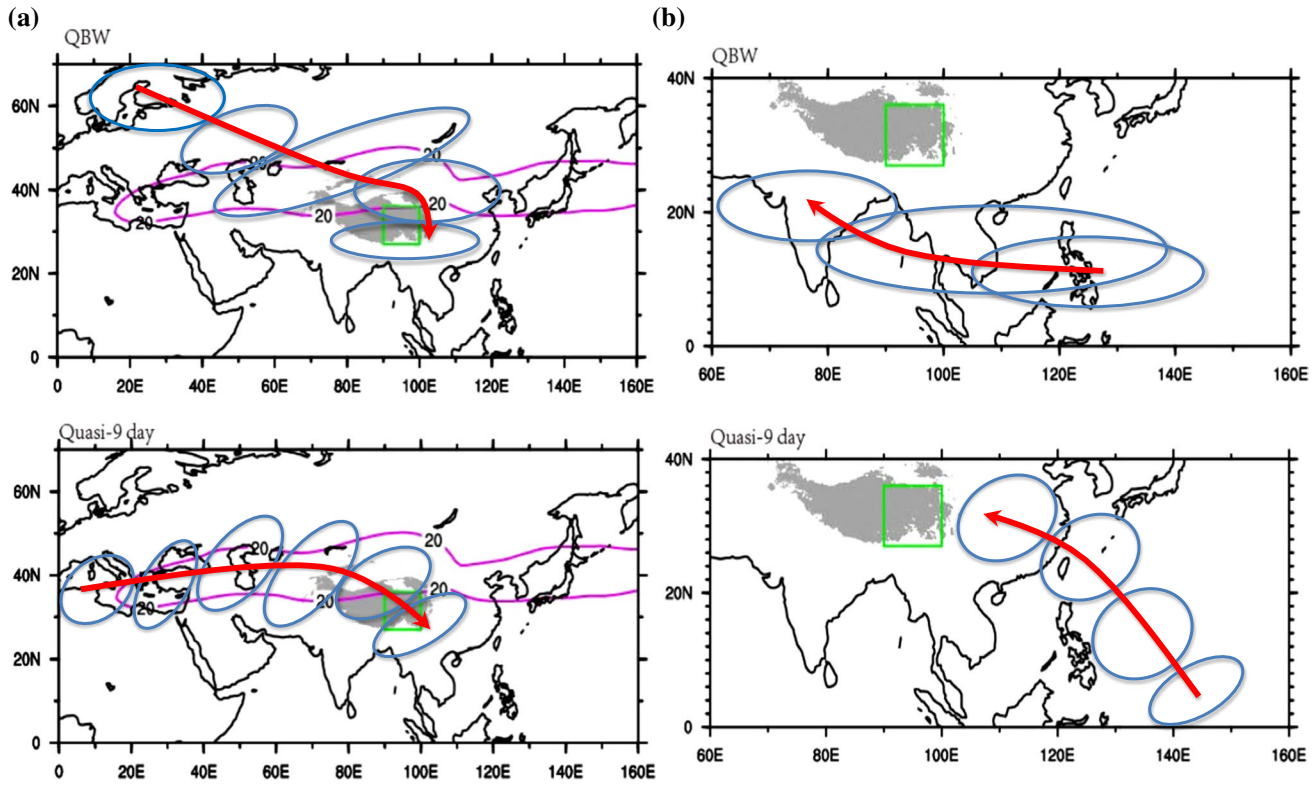

Fig. 14 Schematic diagram for the two major ISV modes over the ETP, summarizing the transient wave trains and propagating paths in both upper- and low-levels. The *blue circle* denotes the major centers of transient anomaly along the wave train propagation. The *green box* is the core region of this study and the *pink* contour is the westerly jet location (20 m/s isoline)

was induced. The positive feedback was addressed as the following: the ascending motion pumped the moisture above the TP from the surroundings, the rising moisture condensed and released latent heat in the mid-troposphere, and then enhanced the baroclinic structure, and finally the upper-level divergence and the low-level convergence induced an extreme wet spell over the ETP. Both the low-level pre-warming and the arrival of the upper-level anticyclonic anomaly were the important preconditions for the ascent anomaly occurrence, which are closely related with upper-level propagating transient wave. The low-level water vapor transport caused the lower tropospheric pre-moistening over southeast of TP, which were directly associated with tropical low-level transient wave propagations. Note that the difference between two modes lies in that the moisture supply primarily came from south of TP for QBW while from east of TP for quasi-9-day mode.

As a summary, although these two ISV periodicities are close with each other, they firstly can be clearly identified from spectrum analysis and they did have different behaviors and structures in the intraseasonal transient wave trains, downstream rainfall patterns, and the large-scale circulations. Therefore, it is necessary to separate these two ISV modes for a better understanding of intraseasonal variation and prediction in the local TP and its surrounding areas.

7 Discussion

According to the above analysis, both ISV modes are closely related with the remarkable co-variabilities respectively in the tropical and mid-latitudes. For QBW, the associated extratropical variability was characterized with a southeastward/southward migratory wave train. And the tropical change featured a northwestward/northward migrating transient wave at the same timescale. These two propagating perturbations encountered over the south of TP. At the extreme wet phase, an upper-level anticyclonic anomaly from the extratropic and a low-level cyclonic anomaly from the tropics interacted over the southern periphery of TP. Their interaction evidently enhanced the southwesterly anomaly over the southern fridge of TP, strengthened the ascending motion and increased the associated water vapor transport. Meanwhile, their encounter enhanced the atmospheric baroclinic structure over ETP at this timescale.

In contrast, for quasi-9-day, the related extratropical variability featured an eastward propagating wave train and the tropical variability exhibited a clear northwestward/westward migration of a wave train. These two wave trains encountered each other over the eastern fridge of TP. At the extreme wet phase, the upper-level anticyclonic anomaly from west and the low-level cyclonic anomaly from east interacted over the east of TP. As a result, the low-level convergence and the ascent anomaly are enhanced over the eastern flank of TP and the local rainfalls are generated. The interaction to the southeast of TP increased the transport of the moisture toward ETP.

The causes for the co-variations of transient atmospheric circulations between tropics and extratropics remained unclear. On one hand, some previous studies had reported that the low-latitude high frequency oscillation was originated from mid-latitudes. For examples, Yang et al. (2010) had proposed the origin of the western Pacific QBW could be attributed to the mid-latitude perturbation when they studied the QBW over East Asia. And Tam and Li (2006) suggested that the summertime high frequency disturbances over tropical western Pacific might originate from the extratropical forcing, because near the date line there was a southward wave activity from the extratropics penetrating into the tropics, which resulted in low-level disturbances that subsequently moved westward in the western Pacific and grew. Their findings all indicated that the generation of the tropical transient migratory wave could come from the mid-latitude transient wave, which cause the covariability between tropics and extratropics. On the other hand, we assumed that the summer heating over TP could induce a Rossby-wave response along the Asian jet, and the strong pumping associated with the peak wet phase over TP could facilitate the northward propagation of convection activity toward TP. Recently, Wang and Duan (2015) consider the moisture advection can destabilize the lower atmosphere which was responsible for the northward propagation of the low-level transient disturbance of QBW. Additionally, Liu et al. (2007) found the local heating itself over TP could induce QBW periodicity in a theoretical model. Therefore, numerical modeling research is needed to investigate the cause of the linkage between the tropics and the mid-latitudes over TP and the effects of TP intraseasonal heating on forming and affecting the circulation non-stationary signals in both mid-latitudes and tropics on intraseasonal times scale.

Acknowledgments This study was supported by funds from the National Natural Science Foundation of China (Grant No. 41375003), the Creative Research Groups of the National Natural Science Foundation of China (No. 41321001). QB thanks the supported from "973" Grant of China (No. 2012GB417203). BW acknowledges the support from Climate Dynamics Program of the National Science Foundation Under Award No NOAA/DYNAMO # NA13OAR4310167 and the National Research Foundation (NRF) of Korea through a Global Research Laboratory (GRL) grant (MEST, #2011-0021927). This is the ESMC publication 109.

References

Annamalai H, Slingo JM (2001) Active/break cycles: diagnosis of the intraseasonal variability of the Asian Summer Monsoon. Clim Dyn 18:85–102

Bingham C, Godfrey MD, Tukey JW (1967) Modern techniques of power spectrum estimation. IEEE Trans 15:56–66

Chen TC, Chen JR (1995) An observational study of the South China Sea Monsoon during the 1979 summer: onset and life cycle. Mon Weather Rev 123:2295–2318

Chou JF, Zheng ZH, Sun SP (2010) The think about 10–30-day extended-range numerical weather prediction strategy-facing the atmosphere chaos. Sci Meteorol Sin 30:569–573 **(in Chinese)**

Ding QH, Wang B (2007) Intraseasonal teleconnection between the Summer Eurasian wave train and the Indian monsoon. J Clim 20:3751–3767

Duan AM, Wu GX, Liu YM, Ma YM, Zhao P (2012) Weather and climate effects of the Tibetan Plateau. Adv Atmos Sci 29:978–992

Dugam SS, Bansod SD, Kakade SB (2009) Pre-monsoon zonal wind index over Tibetan Plateau and sub-seasonal Indian summer monsoon rainfall variability. Geophys Res Lett. doi:10.1029/2009GL038207

Endo N, Ueno K, Yasunari T (1994) Seasonal change of the troposphere in the early summer of 1993 over the central Tibet observed in Tanggula mountains. Bull Glacier Res 12:25–30

Fujinami H, Yasunari T (2004) Submonthly variability of convection and circulation over and around the Tibetan Plateau during the Boreal Summer. J Meteorol Soc Jpn 82:1545–1564

Fujinami H, Yasunari T (2009) The effects of midlatitude waves over and around the Tibetan Plateau on submonthly variability of the East Asian summer monsoon. Mon Weather Rev 137:2286–2304

Gilman DL, Fuglister FJ, Mitchell JM Jr (1963) On the power spectrum of red noise. J Atmos Sci 20:182–184

Huang HY, He JH, Zhu ZW (2011) Advances in research on atmospheric intraseasonal oscillation and its application to extended range forecast. Meteorol Disaster Reduct Res 34:1–8 **(in Chinese)**

Huffman GJ, Adler RF, Morrissey MM, Crutis S, Joyce R, McGavock B, Susskind J (2001) Global precipitation at one-degree daily resolution from multi-satellite observations. J Hydrometeorol 2:36–50

Liu FM, Liu H (1991) Relationships between the atmospheric low-frequency oscillation and the variation of the South Asian High. Plateau Meteor 10:61–69 **(in Chinese)**

Liu YM, Hoskins BJ, Blackburn M (2007) Impact of Tibetan orography oscillation and heating on the summer flow over Asia. J Meteorol Soc Jpn 85:1–19

Liu HB, Yang J, Zhang DL, Wang B (2014) Roles of synoptic to quasi-biweekly disturbances in generating the summer 2003 heavy rainfall in East China. Mon Weather Rev. doi:10.1175/MWR-D-13-00055.1

Mao JY, Chan JCL (2005) Intraseasonal variability of the South China Sea summer monsoon. J Clim 18:2388–2402

Nitta T (1983) Observational study of heat-sources over the Eastern Tibetan Plateau during the summer monsoon. J Meteorol Soc Jpn 61:590–605

Ren RC, Wu GX (2003) On the short-term structure and formation of the subtropical anticyclone in the summer of 1998. Acta Meteorol Sin 61:180–195

Ren RC, Liu YM, Wu GX (2007) Impact of South Asia High on the short -term variation of the subtropical anticyclone over Western Pacific in July 1998. Acta Meteorol Sin 65:183–197 **(in Chinese)**

Ren XJ, Yang DJ, Yang XQ (2015) Characteristics and mechanisms of the subseasonal eastward extension of the South Asian High. J Clim 28:6799–6822

Simmons A, Uppala S, Dee D, Kobayashi S (2007) ERA-Interim: new ECMWF reanalysis products from 1989 onwards. ECMWF Newsl 110:25–35

Tam CY, Li T (2006) The origin and dispersion characteristics of the observed tropical summertime synoptic-scale waves over the western Pacific. Mon Weather Rev 134:1630–1646

Tao SY, Ding YH (1981) Observation evidence of the influence of the Tibet Plateau on the occurrence of heavy rain and severe convective storms in China. Bull Am Meteorol Soc 61:23–30

Wang B, Xu XH (1997) Northern Hemisphere summer monsoon singularities and climatological intraseasonal oscillation. J Clim 10:1071–1085

Wang MR, Duan AM (2015) Quasi-biweekly oscillation over the Tibetan Plateau and its link with the Asian Summer Monsoon. J Clim 28:4921–4940

Wang YN, Chen LX, He JH, Zhang B (2009) Effect of summer heat source low-frequency oscillation over the Tibetan Plateau on precipitation in Eastern China. J Appl Meteorol Sci 20:419–427 **(in Chinese)**

Watanabe T, Yamazaki K (2012) Influence of the anticyclonic anomaly in the subtropical jet over the western Tibetan Plateau on the intraseasonal variability of the summer Asian monsoon in early summer. J Clim 25:1291–1303

Xie P, Yatagai A, Chen M, Hayasaka T, Fukushima Y, Liu C, Yang S (2007) A gauge-based analysis of daily precipitation over East Asia. J Hydrometeorol 8:607–627

Yamada T, Uyeda H (2006) Transition of the rainfall characteristics related to the moistening of the land surface over the central Tibetan Plateau during the summer of 1998. Mon Weather Rev 134:3230–3247

Yang J, Wang B, Wang B (2008) Anticorrelated intensity change of the quasi-biweekly and 30–50-day oscillations over the South China Sea. Geophys Res Lett 35:L16702. doi:10.1029/2008GL034449

Yang J, Wang B, Wang B, Bao Q (2010) Biweekly and 21–30 day variabilities of the subtropical East Asian monsoon over the lower reach of Yangtze River Basin. J Clim 23:1146–1159

Yang J, Bao Q, Gong DY, Wang B (2014) Distinct quasi-biweekly variations of the subtropical East Asian monsoon during early and late summers. Clim Dyn 42:1469–1486

Yasunari T, Miwa T (2006) Convective cloud systems over the Tibetan Plateau and their impact on meso-scale disturbances in the Meiyu/Baiu frontal zone—A case study in 1998. J Meteorol Soc Japan 84:783–803

Yatagai A, Kamiguchi K, Arakawa O, Hamada A, Yasutomi N, Kitoh A (2012) APHRODITE: Constructing a long-term daily gridded precipitation dataset for Asia based on a dense network of rain gauges. Bull Am Meteorol Soc 93:1401–1415

Zhan RF, Li JP (2008) Validation and characteristics of upper tropospheric water vapor over the Tibetan Plateau from AIRS satellite retrieval. Chin J Atmos Sci 32:242–260 **(in Chinese)**

Zhang P, Li JP, Fu X, Liu Y, Li L (2014) Clustering of Tibetan Plateau vortices by 10–30-day intraseasonal oscillation. Mon Weather Rev. doi:10.1175/MWR-D-13-00137.1

Zhou B, He JH, Xu HM (2000) LFO characteristics of meteorological elements over Tibetan Plateau and the relations with regional summer rainfall. J Nanjing Inst Meteorol 23:93–100 **(in Chinese)**